COMPUTATIONAL THERMAL SCIENCES: AN INTERNATIONAL JOURNAL

ASTFE

An Official Journal of the American Society of Thermal and Fluids Engineers

Publisher: Begell House, USA.

ISSN Print: 1940-2503; ISSN Online: 1940-2554

Accepted October 24th 2018

NUMERICAL SOLUTIONS FOR AXISYMMETRIC NON-NEWTONIAN STAGNATION ENROBING FLOW, HEAT AND MASS TRANSFER WITH APPLICATION TO CYLINDRICAL PIPE COATING DYNAMICS

O. Anwar Bég[1], R. Bhargava[2], Sapna Sharma[3], T. A. Bég[4], MD. Shamshuddin[5*] and **Ali Kadir[1]**

[1]*Aeronautical and Mechanical Engineering, University of Salford, Manchester, M54WT,* ***UK.***
[2]*Mathematics Department, Indian Institute of Technology-Roorkee,* ***India.***
[3] *School of Mathematics, Thapar University, Patiala - 147001, Punjab,* ***India.***
[4] *Computational Mechanics and Renewable Energy, Dickenson Road, Manchester, M13,* ***UK.***
[5*]*Department of Mathematics, Vaagdevi College of Engineering, Warangal, Telangana-506005,****India.***
****Corresponding author:*** shammaths@gmail.com

ABSTRACT

Heat and mass transfer in variable thermal conductivity micropolar axisymmetric stagnation enrobing flow on a cylinder is studied. Numerical solutions are obtained with an optimized variational finite element procedure and also a finite difference method. Graphical variations of velocity, angular velocity, temperature and concentration are presented for the effects of Reynolds number, viscosity ratio, curvature parameter, Prandtl number and Schmidt number. Excellent agreement is obtained for both finite element method (FEM) and finite difference method (FDM) computations. Further validation is achieved with a Chebyshev spectral collocation method (SCM). Skin friction is elevated with greater Reynolds number whereas it is suppressed with increasing micropolar parameter. Heat transfer rate decreases with an increase in the thermal conductivity parameter. Temperature and thermal boundary layer thickness is reduced with increasing thermal conductivity parameter and Reynolds number. Greater Reynolds number accelerates the micro-rotation values. Higher Schmidt number reduces the mass transfer function (species concentration) values. The mathematical model is relevant to polymeric manufacturing coating (enrobing) flows.

Keywords: *Micropolar; thermal conductivity; stagnation point; finite element method, enrobing.*

1. Introduction

Fluid mechanics is important in many branches of engineering manufacturing including control of debris materials (Dowding and Lawrence, 2009), nano-materials synthesis (Das et al., 2012) and grinding systems (Mihic et al., 2013; Parthasarthy and Malkin, 2010). Coupled heat and

mass transfer phenomena are also important in a range of enrobing flows in foodstuff and biotechnological material coating systems (Cunningham, 1995; Bean, 2009; Gray, 2009). Mixed convection is in particular a commonly encountered phenomenon and describes situations where both buoyancy and pressure forces exert an influence on the flow domain. Some excellent practical applications are documented in the monograph of (Denn, 1998). Many researchers have investigated coupled heat and mass transfer flows, often employing boundary layer theory to simplify the transport equations in order to yield numerical or closed-form solutions. This generally reduces the elliptic (Navier-Stokes) models to parabolic differential models which are significantly simpler to simulate yet retain a considerably degree of accuracy and physical relevance. Many of the studies communicated have been motivated by applications in polymeric, foodstuff and other process engineering systems. (Tien and Campbell, 1963) examined the combined heat and mass transfer from spinning conical geometries using boundary-layer theory. Heat and mass transfer in the presence of complex physical effects such as hydro magnetism, lateral mass flux, condensing surfaces and so on has also stimulated major investigations in the past several decades owing to significant applications in magnetic materials processing. (Fedrov and Viskanta, 1998) studied the heat and mass transfer and also adsorption aspects in a honeycomb material. (Dietl et al., 1998) numerically investigated the heat and mass transfer in hygroscopic material drying processes. A coupled heat and transfer mathematical model for an adsorption reactor was presented by (Fedrov and Viskanta, 1999). Further interesting studies of relevance to manufacturing engineering have been presented by (Grigoropoulos et al., 1996) for pulsed-laser-induced material modification, (Bég et al., 2009) for magnetohydrodynamic sheet processing, (Tan et al., 2012) for laser spot conduction welding, (Uddin et al., 2013) for rheological nanogel thermal processing and (Rashidi et al., 2012) for combustion boundary layers. Clearly there is a wide interest in heat and mass transfer processes. For coupled problems (involving

buoyancy), the differential equations are more complex to solve, and numerical methods are the only practicable means to yield solutions of interest to the engineering science community. All these studies have been concerned with Navier-Stokes or *Newtonian* fluids. However, there are many environmental and industrial flows where the transport fluid deviates substantially in behaviour from this classical theory. *Non-Newtonian* fluid models are therefore needed to analyze such flow domains. Many such models have been communicated and are reviewed in the excellent monograph by (Edwards and Brenner, 1993). Among the generalized theories for rheological fluids, the most comprehensive has proven to be that of the *micromorphic fluid* introduced in a classical paper by (Eringen, 1964). The theory of micropolar fluids was developed due to the increasing importance in processing industries and elsewhere of materials which have significant micro-structural characteristics including couple stresses and rotating elements at the microscopic level. Experiments done by (Hoyt and Fabula, 1964), with fluid containing a minute number of polymeric additives indicate a reduction in skin friction near a rigid body, when compared with the skin friction in the same fluid without additives. This phenomenon *cannot* be explained on the basis of the so-called viscoelastic family of rheological models. In support of these experiments, (Eringen, 1966) proposed the theory of micropolar fluids, which took in to account the initial characteristics of the substructure particles, which are allowing to undergo rotation. The theory can be applied successfully to explain the colloidal fluids, foodstuffs (chocolate), liquid crystals fluid with additives and many other "complex fluids". Later (Eringen. 1972) developed the theory of thermo-micropolar fluids to include heating effects. The study of heat and mass transfer in micropolar liquids has important applications including extrusion flows (Kelson and Farrell, 2001), energy systems (Rawat et al., 2009), polymeric synthesis (Bég et al., 2010) and medical engineering (Rashidi et al., 2011). Micropolar transport phenomena therefore are important to study from the viewpoint of elucidating more accurately the flow dynamics occurring in many manufacturing

engineering systems. A great amount of research in micropolar hydromechanics and heat transfer has been communicated in the past three decades. For example, (Gorla and Hassanien, 1990) studied the boundary flow of a micropolar fluid near the stagnation point on a horizontal cylinder. This analysis was extended for the case of heat transfer by (Hassanien and Salma, 1997). (Mansoor et al., 2000) studied the heat and mass transfer in MHD flow of a micropolar fluid on a circular cylinder with uniform heat and mass transfer. (Bég et al., 2008) recently studied the biomagnetic micropolar heat transfer in a non-Darcian biomaterial. (Zueco et al., 2009) have investigated the magneto-micropolar convection through a vertical circular non-Darcian porous medium conduit. Other recent studies of multi-physical micropolar flows include (Mishra et al., 2015) (on magnetic natural convection micropolar flow with heat generation), (Rout et al., 2016) (on reactive magnetic natural convection micropolar boundary layers), (Mishra et al., 2016) (cross diffusion in magnetic Sakiadis micropolar flow), (Baag et al., 2017) (on stagnation chemically-reacting magnetized micropolar convection with internal heat generation). Further studies of relevance are (Mehmood et al., 2017) (on viscoplastic micropolar Sakiadis convection flow), (Iqbal et al., 2017) (on finite difference analysis of hydromagnetic oblique micropolar flow) and (Mehmood et al., 2016) on rotating channel magneto-micropolar convection). All these investigations confirmed the substantial modification in heat and momentum transfer characteristics computed by including micro-structural effects. These studies were based on micropolar fluids possessing constant physical properties such as viscosity and thermal conductivity. However, these properties in real problems are greatly affected due to high temperature. In particular the influence of variable thermal conductivity finds significant applications in *enrobing* flows. The variable fluid property for viscous and incompressible fluids was first analyzed by (Ghaly and Seedeek, 2002) etc. Very little work has been done in this direction for the case of micropolar fluids. Additionally, the importance of species diffusion of micropolar fluids has also been neglected

in many studies despite the importance of this effect in sedimentary interaction with diffusing contaminants in the coastal/ocean zone, electroplating technologies in the metallurgical industries etc. In the present paper, we therefore investigate the boundary layer stagnation flow heat and species transfer of a micropolar fluid past a horizontal cylinder with variable thermal conductivity effects. The governing differential equations are reduced to nonlinear simultaneous differential equations by using similarity transformations. These equations are solved using an optimized finite element method, robust finite difference technique and a Chebyshev spectral collocation algorithm. The effect of variable thermal conductivity parameter, Reynolds number and Schmidt number are studied on the flow, heat and mass transfer fields graphically. Excellent validation of the computations is demonstrated.

2. Hydrodynamics of Micropolar Fluids

Prior to developing the mathematical model for the flow regime under consideration we shall initially discuss briefly the mechanics of micropolar fluids, to provide the reader not familiar with this theory with a physical insight into its formulation. Micropolar fluids are a special sub-class of simple microfluids. These fluids exhibit behaviour and properties which are influenced by the local motions of the material particles contained in each of the volume elements i.e. microelements. They possess local inertia. The simple microfluids are isotropic viscous fluids and in the linear case are characterized by twenty-two viscosity coefficients. Such “simple” fluids require a system of nineteen partial differential equations with nineteen unknowns to simulate completely. As such the micropolar model reduces this complex system to seven equations, three for translational motion, three for angular momentum and a conservation of mass equation. Micropolar fluids have volume elements containing rigid particles (non-deformable) which can spin about the center of the volume element and are defined by a micro-rotation vector. This local rotation of the particles is supplementary to the conventional rigid

body motion of the entire volume element which defines Navier-Stokes fluids. In micropolar fluid mechanics, the classical continuum laws are therefore augmented with additional equations which account for the conservation of micro-inertia moments and the balance of first stress moments which arise due to the consideration of micro-structure in a fluid. Hence new kinematic variables (gyration tensor, microinertia moment tensor), and concepts of body moments, stress moments and micro-stress are amalgamated with classical continuum fluid dynamics theory. The field equations for micropolar fluids in generalized form can be stated following (Eringen, 2002) as follows:

Conservation of Mass

$$\frac{\partial \rho}{\partial t} + \nabla \bullet (\rho \mathbf{V}) = 0 \tag{1}$$

Conservation of Translational Momentum

$$\left(\lambda+2\mu+\kappa\right)\nabla\nabla \bullet V - \left(\mu+\kappa\right)\nabla\times\nabla\times V + \kappa\,\nabla\times G - \nabla P + \rho f = \rho V \tag{2}$$

Conservation of Angular Momentum (Micro-rotation)

$$\left(\alpha+\beta+\gamma\right)\nabla\nabla \bullet G - \gamma\,\nabla\times\nabla\times G + \kappa\,\nabla\times V - 2\kappa G + \rho\, l = \rho\, j\, G \tag{3}$$

where ρ the mass density of micropolar fluid, V is translational velocity vector, G is angular velocity (microrotation or gyration) vector, j is microinertia, f is the body force per unit mass vector, *l* is the body couple per unit mass vector, p is the thermodynamic pressure, μ is the Newtonian dynamic viscosity, λ is the Eringen second order viscosity coefficient, κ is the vortex viscosity coefficient, and α, β and γ are spin gradient viscosity coefficients for micropolar fluids. In the micropolar model theory we are only concerned with two independent kinematical vector fields, namely the velocity vector field (familiar from Navier-Stokes theory) and the axial vector field which simulates the spin or the microrotations of the micropolar fluid particles, these being assumed non-deformable i.e. rigid. We apply this model to the two-dimensional boundary layer flow past a horizontal infinite cylinder as illustrated in Schematic 1. We note that in micropolar fluid theory for the case where the fluid has constant physical

properties, no external body forces exist and for steady state flow, the conservation equations can be greatly simplified. Additionally, for the case where $\kappa = \alpha = \beta = \gamma = 0$ and with vanishing l and f, the gyration vector disappears and equation (2.3) due to (Eringen, 2002) vanishes. Equation (2) also reduces in this special case to the classical Navier-Stokes equations. We also note that for the case of zero vortex viscosity only, the velocity vector ***V*** and the micro-rotation ***G*** are decoupled, and the global motion is unaffected by the micro-rotations.

3. Mathematical Model

Consider the steady, incompressible micropolar heat and mass transfer in boundary layer flow at a stagnation point on an infinite horizontal circular cylinder of diameter 2a, with reference to a cylindrical (r, ϕ, z) coordinate system. The regime is illustrated in schematic 1. The species is assumed to be a non-reactive second fluid diffusing within the micropolar ambient fluid medium, as encountered for example in a pollutant released from a horizontal pipeline. We neglect turbulent and oscillatory flow effects. The flow is also assumed to be axisymmetric about the z-axis and also symmetric to the r-ϕ plane with the stagnation point located at z = 0. Under the boundary layer approximations, the governing equations can be written as follows:

Continuity

$$\frac{\partial(ru)}{\partial r} + \frac{\partial(rw)}{\partial z} = 0 \tag{4}$$

Radial Translational Momentum:

$$\rho\left(u\frac{\partial u}{\partial r} + w\frac{\partial u}{\partial z}\right) = -\frac{\partial p}{\partial r} + (\mu + K)\left(\frac{\partial}{\partial r}\left(\frac{1}{r}\frac{\partial}{\partial r}(ru)\right) + \frac{\partial^2 u}{\partial z^2}\right) - K\frac{\partial N}{\partial z}, \tag{5}$$

Azimuthal Translational Momentum:

$$\rho\left(u\frac{\partial v}{\partial r} + \frac{uv}{r} + w\frac{\partial v}{\partial z}\right) = (\mu + K)\left(\frac{\partial}{\partial r}\left(\frac{1}{r}\frac{\partial}{\partial r}(rv)\right) + \frac{\partial^2 v}{\partial z^2}\right), \tag{6}$$

Axial Translational Momentum:

$$\rho\left(u\frac{\partial w}{\partial r} + w\frac{\partial w}{\partial z}\right) = -\frac{\partial p}{\partial z} + (\mu + K)\left(\frac{1}{r}\frac{\partial}{\partial r}\left(r\frac{\partial w}{\partial r}\right) + \frac{\partial^2 w}{\partial z^2}\right) + K\left(\frac{\partial N}{\partial r} + \frac{N}{r}\right) \tag{7}$$

Angular momentum (Micro-rotation Conservation):

$$\rho\left(u\frac{\partial N}{\partial r}+w\frac{\partial N}{\partial z}\right)=\frac{\gamma}{j}\left(\frac{\partial}{\partial r}\left(\frac{1}{r}\frac{\partial}{\partial r}(rN)\right)+\frac{\partial^2 N}{\partial z^2}\right)+\frac{K}{j}\left(\frac{\partial u}{\partial z}-\frac{\partial w}{\partial r}-2N\right), \tag{8}$$

Energy (Heat Conservation)

$$\rho\left(u\frac{\partial T}{\partial r}+w\frac{\partial T}{\partial z}\right)=\frac{1}{c_p}\frac{1}{r}\frac{\partial}{\partial r}\left(rK_f\frac{\partial T}{\partial r}\right), \tag{9}$$

Diffusion (Species Conservation)

$$\rho\left(u\frac{\partial C_A}{\partial r}+w\frac{\partial C_A}{\partial z}\right)=\frac{1}{c_p}\frac{k_g}{r}\frac{\partial}{\partial r}\left(r\frac{\partial C_A}{\partial r}\right) \tag{10}$$

The appropriate boundary conditions on the surface of the cylinder and far from the surface in the body of surrounding micropolar fluid are:

At $r=a,$

$$u=0,\quad v=0,\ w=0,\ N=-s\frac{\partial w}{\partial r},\quad T=T_w,\ C_A=C_{Aw}\ , \tag{11a}$$

As $r\to\infty,$

$$u=-A\left(r-\frac{a^2}{r}\right),\qquad v=\frac{Aa^2}{r},\ w=2Az,\ N=-s\frac{\partial w}{\partial r},\quad T=T_\infty,\ C_A=C_{A\infty} \tag{11b}$$

In the above equations (4) to (10), u denotes translational velocity along the r-direction (radial component), v is the translational velocity along the ϕ- direction (tangential or azimuthal component), w is the translational velocity along the z- direction (axial component), ρ is the mass density of micropolar fluid, p is the hydrodynamic pressure, μ is the Newtonian dynamic viscosity, κ is the Eringen vortex viscosity coefficient, N is the angular velocity (micro-rotation) component in the r-z plane, γ is the Eringen spin gradient viscosity, j is microinertia, T is fluid temperature, c_p denotes specific heat at constant pressure (isobaric), K_f is thermal conductivity of the micropolar fluid, C_A is species concentration, k_g is the mass diffusivity of the species (contaminant). In the boundary conditions (11a) and (11b), A is a generalized parameter, C_{Aw} and T_w denote the concentration and temperature at the cylinder wall, $C_{A\infty}$ and

T_∞ designate the concentration and temperature far away from the wall. The variation of the thermal conductivity, K_f, with temperature can be taken for the micropolar fluid as follows:

$$K_f = K_\infty(1 + b(T - T_\infty)) \tag{12}$$

or

$$K_f = K_\infty(1 + \beta\theta) \text{ Where } \beta = b(T_w - T_\infty) \tag{13}$$

where β represents the thermal conductivity parameter. Here b is the conductivity coefficient (a constant) for a particular fluid e.g. $b > 0$ for water and air whereas $b < 0$ for fluids such as oils and petroleum derivatives, as noted in Schlichting (1979). A linear relationship between microrotation function N and the surface shear stress $\partial w / \partial r$ is chosen for investigating the influence of different cylinder surface conditions for the microrotation. Here is the boundary condition parameter and varies from 0 to 1. The boundary condition corresponding to s = 0 corresponds to the no-slip condition i.e. the fluid particles closest to a solid boundary adhere to it, neither translating nor rotating. The second boundary condition, corresponding to $s \neq 0$, implies that in the neighborhood of the rigid boundary (i.e. cylinder surface), the effect of microstructure is negligible since the suspended particles cannot get closer to the boundary than their radius. Hence in the neighborhood of the boundary, the only rotation is due to fluid shear and therefore, the gyration vector must be equal to fluid vorticity, corresponding to $s = -0.5$.

4. Transformation of the Model

To facilitate a numerical solution and generate computations which are independent of the dimensions of the regime i.e. can be applied to any similar geometry, we introduce a set of similarity transformation, following (Gorla and Hassanien, 1990), so that the mass conservation equation (4) is satisfied identically:

$$\eta = \left(\frac{r}{a}\right)^2,\ \theta(\eta) = \frac{T - T_\infty}{T_w - T_\infty},\ N = \left(\frac{A}{a}\right) z\eta^{1/2} g(\eta), \quad u = -Aa\eta^{-1/2} f(\eta),$$
$$v = -Aa\eta^{-1/2} h(\eta),\ w = 2Azf'(\eta),\ \phi = \phi(\eta) = \left(\frac{C_A - C_{A_\infty}}{C_{A_w} - C_{A\infty}}\right) \tag{14}$$

Equation (4) is satisfied identically. Since the radius of the cylinder has been assumed to be very small as compared to other dimension, equation (2) i.e. radial momentum is neglected in the transformation. Equations (4) - (10) are thereby reduced to the following simultaneous ordinary differential equations:

Azimuthal Momentum Equation:

$$(1+R)\eta\Omega'' + \mathrm{Re}\, f\, \Omega' = 0 \tag{15}$$

Axial Momentum Equation:

$$(1+R)(\eta f''' + f'') + \left(\frac{R}{4}\right)(\eta g' + g) + \mathrm{Re}(ff'' - (f')^2) = 0 \tag{16}$$

Angular Momentum (Micro-rotation) Equation:

$$\lambda(\eta^2 g'' + 2\eta g') - BR(\eta f'' + \frac{\eta}{2} g) - \frac{\mathrm{Re}}{2}(2\eta(f'g - fg') - fg) = 0 \tag{17}$$

Energy Equation

$$(1+\beta\theta)(\eta\theta'' + \theta') + \beta\eta(\theta')^2 + \mathrm{Re}\frac{\mathrm{Pr}}{2}(f\theta') = 0 \tag{18}$$

Species Diffusion Equation

$$(\eta\phi'' + \phi') + \mathrm{Re}\frac{Sc}{2}(f\phi') = 0 \tag{19}$$

The corresponding transformed boundary conditions are now:

$$f(1) = 0, \quad f'(1) = 0, \quad \Omega(1) = 0,\ g(1) = -sf''(1),\ \theta(1) = 1,\ \phi(1) = 1,$$
$$f'(\infty) = 1, \quad \Omega(\infty) = 1, \quad g(\infty) = 0 \quad \theta(\infty) = 0, \quad \phi(\infty) = 0 \tag{20}$$

where the prime denotes differentiation with respect to η, $\mathrm{Re} = Aa^2/2\nu$ the Reynolds number, $R = K/\rho\nu$ is the micropolar parameter, $\lambda = \gamma/\rho j$ is the spin-gradient micropolar parameter, $\mathrm{Pr} = \rho c_p \nu / K_\infty$ is the Prandtl number, $\nu = \mu/\rho$ is kinematic viscosity, $B = a^2/j$ the curvature parameter, f is dimensionless stream function, g is dimensionless microrotation, $f' = h$ is dimensionless axial velocity, Ω is dimensionless azimuthal velocity,

$Sc = \rho c_p \nu / k_g$ is Schmidt number, s is the surface parameter, θ is the dimensionless temperature function, ϕ is dimensionless mass transfer function and ∞ designates conditions far away from the surface. In engineering simulations, we are interested not only in the velocity, micro-rotation, temperature and species transfer fields, but also certain gradient functions of these variables. We therefore also define a shear stress at the boundary as follows:

$$\tau_w = \left((\mu + K) \frac{\partial w}{\partial r} + KN \right)_{r=a} = \left(\mu - \frac{K}{2} \right) \left(\frac{4Az}{a} \right) f''(1), \tag{21}$$

The heat flux may also be computed from the following expression:

$$q_w = -k_f \left(\frac{\partial T}{\partial r} \right)_{r=a} = -\frac{2K_f}{a} (T_w - T_\infty) \theta'(1) \tag{22}$$

Finally, the Nusselt number, can be defined as:

$$Nu_z = \frac{z q_w}{K_f (T_w - T_\infty)} = -2 \left(\frac{\mathrm{Re}_z}{\mathrm{Re}} \right)^{1/2} \theta'(1) \tag{23}$$

Where

$$\mathrm{Re}_z = Az^2 / 2\nu \tag{24}$$

5. Finite Element Method (FEM) Solutions

This popular technique (Reddy, 1985) has been employed by the authors in many complex multi-physical industrial flow problems including nanofluid dynamics (Rana et al., 2013a), membrane stress dynamics (Rana et al., 2013b) and stretching sheet rheological flows (Gupta et al., 2014). Here we utilize the variational formulation, also known as the "weak formulation" in computational mechanics (Reddy, 1985).

5.1 Method of solution:

To solve the differential equations (15) - (19) with boundary conditions (20), we assume

$$f' = h, \tag{25}$$

The entire two-point boundary value problem then reduces to:

$$(1 + R) \eta \Omega'' + \mathrm{Re}\, f \Omega' = 0, \tag{26}$$

$$(1+R)(\eta h''+h')+\left(\frac{R}{4}\right)(\eta g'+g)+\mathrm{Re}(fh'-(h')^2)=0, \tag{27}$$

$$\lambda(\eta^2 g''+2\eta g')-BR(\eta f''+\frac{\eta}{2}g)-\frac{\mathrm{Re}}{2}(2\eta(f'g-fg')-fg)=0, \tag{28}$$

$$(1+\beta\theta)(\eta\theta''+\theta')+\beta\eta(\theta')^2+\mathrm{Re}\,\mathrm{Pr}(f\theta')=0, \tag{29}$$

$$(\eta\phi''+\phi')+\mathrm{Re}\,Sc(f\phi')=0, \tag{30}$$

$$\begin{aligned} &f(1)=0,\quad h(1)=0,\quad g(1)=-sf''(1),\quad \Omega(1)=0,\quad \theta(1)=1,\quad \phi(1)=1,\\ &h(\infty)=0,\quad g(\infty)=0,\quad \Omega(\infty)=1,\quad \theta(\infty)=0,\quad \phi(\infty)=0, \end{aligned} \tag{31}$$

The whole domain is divided into eighty-two-noded line elements, over each of the element, finite element equations are derived.

5.2 Variational formulation:

The variational form associated with equation (25) - (30) over a typical linear element (η_e,η_{e+1}) is given by:

$$\int_{\eta_e}^{\eta_{e+1}} w_1(f'-h)\,d\eta=0 \tag{32}$$

$$\int_{\eta_e}^{\eta_{e+1}} w_4((1+R)\eta\Omega''+\mathrm{Re}(f\Omega'))d\eta=0 \tag{33}$$

$$\int_{\eta_e}^{\eta_{e+1}} w_2((1+R)(\eta h''+h')+\left(\frac{R}{4}\right)(\eta g'+g)+\mathrm{Re}(fh'-(h)^2)d\eta=0 \tag{34}$$

$$\int_{\eta_e}^{\eta_{e+1}} w_{3(}\lambda(\eta^2 g''+2\eta g')-BR(\eta f''+\frac{\eta}{2}g)-\frac{\mathrm{Re}}{2}(2\eta(f'g-fg')-fg))d\eta=0 \tag{35}$$

$$\int_{\eta_e}^{\eta_{e+1}} w_5((1+\beta\theta)(\eta\theta''+\theta')+\beta\eta(\theta')^2+\mathrm{Re}\,\mathrm{Pr}(f\theta'))d\eta=0 \tag{36}$$

$$\int_{\eta_e}^{\eta_{e+1}} w_6((\eta\phi''+\phi')+\mathrm{Re}\,Sc(f\phi'))d\eta=0 \tag{37}$$

where $w_{1,}w_2,w_3,w_4,w_5,$ and w_6 are arbitrary test function and may be viewed as the variation in f,h,Ω,g,θ and ϕ respectively.

5.3 Implementation of the Finite Element Method:

Finite element formulation:

The finite element model is for equations obtained after variation formulation by substituting finite element approximation of the following form

$$\Omega=\sum_{j=1}^{2}\Omega_j\xi_j,\ f=\sum_{j=1}^{2}f_j\xi_j,\ h=\sum_{j=1}^{2}h_i\xi_i,\quad g=\sum_{j=1}^{2}g_j\xi_j,\theta=\sum_{j=1}^{2}\theta_j\xi_j,\ \phi=\sum_{j=1}^{2}\phi_j\xi_j \tag{38}$$

where $w_i=\xi_1,$ for the first node and $w_i=\xi_2,$ for the second node with $i=1,2,3,4,5,6$

Here ξ_j are the shape functions for the line element (η_e,η_{e+1}) and are taken as:

$$\xi_1^{\,e}=\frac{\eta_{e+1}-\eta}{\eta_{e+1}-\eta_e},\ \ \xi_2^{e}=\frac{\eta-\eta_e}{\eta_{e+1}-\eta_e}\ \text{where}\ \eta_e\le\eta\le\eta_{e+1} \tag{39}$$

The finite element model of the equation (32)-(37) for the typical element thus formed is given by:

$$\begin{bmatrix}[K^{11}]&[K^{12}]&[K^{13}]&[K^{14}]&[K^{15}]&[K^{16}]\\ [K^{21}]&[K^{22}]&[K^{23}]&[K^{24}]&[K^{25}]&[K^{26}]\\ [K^{31}]&[K^{32}]&[K^{33}]&[K^{34}]&[K^{35}]&[K^{36}]\\ [K^{41}]&[K^{42}]&[K^{43}]&[K^{44}]&[K^{45}]&[K^{46}]\\ [K^{51}]&[K^{52}]&[K^{53}]&[K^{54}]&[K^{55}]&[K^{56}]\\ [K^{61}]&[K^{62}]&[K^{63}]&[K^{64}]&[K^{65}]&[K^{66}]\end{bmatrix}\begin{bmatrix}\{f\}\\ \{h\}\\ \{g\}\\ \{\Omega\}\\ \{\theta\}\\ \{\phi\}\end{bmatrix}=\begin{bmatrix}\{r^1\}\\ \{r^2\}\\ \{r^3\}\\ \{r^4\}\\ \{r^5\}\\ \{r^6\}\end{bmatrix} \tag{40}$$

Here each $\left[K^{mn}\right]$ is of the order 2×2 and $\left[r^m\right]$ $(m,n=1,2,3,4,5,6)$ is of 2×1. These matrices are defined as:

$$K_{ij}^{11}=\int_{\eta_e}^{\eta_{e+1}}\xi_i\frac{d\xi_j}{d\eta}d\eta,\ \ K_{ij}^{12}=-\int_{\eta_e}^{\eta_{e+1}}\xi_i\xi_j d\eta,$$
$$K_{ij}^{13}=K_{ij}^{14}=K_{ij}^{15}=K_{ij}^{16}=0 \tag{41}$$

$$K_{ij}^{21}=0,\ K_{ij}^{22}=-(1+R)\int_{\eta_e}^{\eta_{e+1}}\eta\frac{d\xi_i}{d\eta}\frac{d\xi_j}{d\eta}d\eta+\mathrm{Re}\int_{\eta_e}^{\eta_{e+1}}\xi_i\,\overline{f}\,\frac{d\xi_i}{d\eta}d\eta-\mathrm{Re}\int_{\eta e}^{\eta_{e+1}}\overline{h}\xi_i\xi_j d\eta$$
$$K_{ij}^{23}=\frac{R}{4}\int_{\eta_e}^{\eta_{e+1}}\eta\xi_i\frac{d\xi_j}{d\eta}d\eta+\frac{R}{4}\int_{\eta_e}^{\eta_{e+1}}\xi_i\xi_j d\eta,\qquad K_{ij}^{24}=\ K_{ij}^{25}=K_{ij}^{26}=0 \tag{42}$$

$$K_{ij}^{31}=0,\ K_{ij}^{32}=-BR\int_{\eta_e}^{\eta_{e+1}}\eta\xi_i\frac{d\xi_j}{d\eta}d\eta,$$

$$K_{ij}^{33}=-\lambda\int_{\eta_e}^{\eta_{e+1}}(2\eta\xi_i\frac{d\xi_i}{d\eta}+\eta^2\frac{d\xi_i}{d\eta}\frac{d\xi_j}{d\eta})d\eta-2\lambda\int_{\eta_e}^{\eta_{e+1}}\eta\xi_i\frac{d\xi_j}{d\eta}-\frac{BR}{2}\int_{\eta_e}^{\eta_{e+1}}\eta\xi_i\xi_j d\eta$$
$$-\mathrm{Re}\int_{\eta_e}^{\eta_{e+1}}\overline{\Omega\eta}\xi_i\xi_j d\eta+\mathrm{Re}\int_{\eta_e}^{\eta_{e+1}}\overline{f}\,\eta\xi_i\frac{d\xi_i}{d\eta}d\eta+\frac{\mathrm{Re}}{2}\int_{\eta_e}^{\eta_{e+1}}\overline{f}\xi_i\xi_j d\eta \quad (43)$$

$$K_{ij}^{34}=K_{ij}^{35}=K_{ij}^{36}=0$$

$$K_{ij}^{41}=K_{ij}^{42}=K_{ij}^{43}=0,$$

$$K_{ij}^{44}=(1+R)\int_{\eta_e}^{\eta_{e+1}}\eta\frac{d\xi_i}{d\eta}\frac{d\xi_j}{d\eta}d\eta+\int_{\eta_e}^{\eta_{e+1}}\xi_i\frac{d\xi_j}{d\eta}d\eta+\mathrm{Re}\int_{\eta_e}^{\eta_{e+1}}\overline{f}\xi_i\frac{d\xi_j}{d\eta}d\eta, \quad (44)$$

$$K_{ij}^{45}=K_{ij}^{46}=0,$$

$$K_{ij}^{51}=K_{ij}^{52}=K_{ij}^{53}=K_{ij}^{54}=0,$$

$$K_{ij}^{55}=\int_{\eta_e}^{\eta_{e+1}}\xi_i\frac{d\xi_j}{d\eta}d\eta-\int_{\eta_e}^{\eta_{e+1}}\left\{\eta\frac{d\xi_i}{d\eta}\frac{d\xi_j}{d\eta}+\beta\xi_i\overline{\theta}\frac{d\xi_j}{d\eta}+\beta\eta\xi_i\overline{\theta}\frac{d\xi_j}{d\eta}\right\}d\eta \quad (45)$$
$$+\mathrm{Re}\,\mathrm{Pr}\int_{\eta_e}^{\eta_{e+1}}\overline{f}\xi_i\frac{d\xi_j}{d\eta}d\eta,$$

$$K_{ij}^{61}=K_{ij}^{62}=K_{ij}^{63}=K_{ij}^{64}=K_{ij}^{65}=0,$$

$$K_{ij}^{66}=-\int_{\eta_e}^{\eta_{e+1}}\xi_i\frac{d\xi_j}{d\eta}d\eta-\int_{\eta_e}^{\eta_{e+1}}\left\{\eta\frac{d\xi_i}{d\eta}\frac{d\xi_j}{d\eta}\right\}d\eta+\mathrm{Re}\,Sc\int_{\eta_e}^{\eta_{e+1}}\overline{f}\xi_i\frac{d\xi_j}{d\eta}d\eta \quad (46)$$

$$r_i^1=0,\qquad r_i^2=-\left(\xi_i\frac{dh}{d\eta}\right)_{\eta_e}^{\eta_{e+1}},\quad r_i^3=\left(\xi_i\frac{dg}{d\eta}\right)_{\eta_e}^{\eta_{e+1}},$$
$$r_i^4=-\left(\xi_i\frac{d\Omega}{d\eta}\right)_{\eta_e}^{\eta_{e+1}},r_i^5=-\left(\xi_i\frac{d\theta}{d\eta}\right)_{\eta_e}^{\eta_{e+1}},r_i^6=-\left(\xi_i\frac{d\phi}{d\eta}\right)_{\eta_e}^{\eta_{e+1}} \quad (47)$$

where

$$\overline{f}=\sum_{j=1}^{2}\overline{f_j}\xi_j,\ \overline{h}=\sum_{j=1}^{2}\overline{h_j}\xi_j,\ \overline{\Omega}=\sum_{j=1}^{2}\overline{\Omega_j}\,\xi_j and\ \overline{\theta}=\sum_{j=1}^{2}\overline{\theta_j}\xi_j \quad (48)$$

The whole domain is divided in to a set of 80-line elements. Each element matrix is of order 12×12. Thus after assembly of all the element equations we obtained a matrix of order 486×486. For the computation purpose η_∞ has been fixed at 40, since all the unknown functions attained the desired accuracy of 0.0005. If η_∞ is taken more than 40, all the above functions do

not change up to the desired accuracy. The system of equations as obtained after assembly of the element equations, is nonlinear therefore an iterative scheme has been used to solve it. The system is linearized (Rana et al., 2013a; Rana et al., 2013b; Gupta et al., 2014) by incorporating the known functions $\overline{f}, \overline{h}, \overline{\Omega},$ and $\overline{\theta}$.

6. Finite Difference Method (FDM) Solutions

For validation of the present FEM code, the same system of nonlinear coupled differential equations (25)– (30), subject to boundary conditions (31) are solved numerically using the finite difference method **(FDM).** No viable solutions from the literature are available with which to make a robust comparison. The advantage of using an alternative method is that the full model can be verified, not just a simpler version of it. The FDM method is equally efficient for ordinary as well as partial differential equations of the boundary value type or initial value type. Employing central-difference formulae, the set of equations (25)– (30), can be written as follows:

$$h_i = \frac{f_{i+1} - f_{i+1}}{2h_e} \tag{49}$$

$$(1+R)\left(\eta_i\left(\frac{(h_{i+1} - 2h_i + h_{i-1})}{he^2}\right) + \frac{(h_{i+1} - h_{i-1})}{2he}\right) + \left(\frac{R}{4}\right)\left(\eta_i\left(\frac{(g_{i+1} - g_{i-1})}{2he} + g_i\right)\right) + \text{Re}\left(\left(f_i\left(\frac{(h_{i+1} - h_{i-1})}{2he}\right)\right) - (h_i)^2\right) = 0, \tag{50}$$

$$(1+R)\left(\eta_i\left(\frac{\Omega_{i+1} - 2\Omega_i + \Omega_{i-1}}{h_e^{\,2}}\right)\right) + \text{Re}\, f_i\left(\frac{\Omega_{i+1} - \Omega_{i-1}}{2h_e}\right) = 0, \tag{51}$$

$$\lambda\left(\eta_i^{\,2}\left(\frac{(g_{i+1}-2g_i+g_{i-1})}{he^2}\right)+2\eta_i g_i\right)-BR(\eta_i\left(\frac{(f_{i+1}-2f_i+f_{i-1})}{he^2}\right)+$$
$$\frac{\eta_i}{2}g_i)-\frac{\mathrm{Re}}{2}\left(2\eta_i(h_i g_i-f_i\left(\frac{g_{i+1}-g_{i-1}}{2h_e}\right)-f_i g_i\right)=0, \tag{52}$$

$$(1+\beta\theta_i)\left(\eta_i\left(\frac{(\theta_{i+1}-2\theta_i+\theta_{i+1})}{h_e^{\,2}}\right)+\theta'\right)+\beta\eta_i\left(\frac{\theta_{i+1}-\theta_{i-1}}{2h_e}\right)^2+\mathrm{Re}\,\mathrm{Pr}\left(f_i\left(\frac{\theta_{i+1}-\theta_{i-1}}{2h_e}\right)\right)=0, \tag{53}$$

$$\left(\eta_i\left(\frac{\phi_{i+1}-2\phi_i+\phi_{i-1}}{h_e^{\,2}}\right)+\left(\frac{\phi_{i+1}-\phi_{i-1}}{2h_e}\right)\right)+\mathrm{Re}\,Sc\left(f_i\left(\frac{\phi_{i+1}-\phi_{i-1}}{2h_e}\right)\right)=0, \tag{54}$$

where h_e is the step length. Since the above equations are non–linear and coupled hence they cannot be solved exactly. Therefore, an iterative scheme is required to be used. Writing down the equations in the form:

$$x_i=F\left(l_1,l_2,\ \ldots\ \ldots\ \ldots\ l_n\right) \tag{55}$$

where each l_i is the function of the variable $f_i,h_i,\Omega_i,g_i,\theta_i,\phi_i$ and x_i is any of the variable $f_i,h_i,\Omega_i,g_i,\theta_i,\phi_i$. Similar type of equations is written for each variable of the equations (49)–(54). Now starting with initial guess values, new iterate values are obtained. This process continues till the absolute error $\left|x_i-x_{i-1}\right|$ is less than the accuracy required. The condition of convergence of the scheme has been already checked before implementing the iterative scheme. More details are to be found in (Bég et al., 2011). Following equation (55), the equations (49)-(54) can be written as follows:

$$f_{i+1}=h_i 2h_e+f_i \tag{56}$$

$$h_i=\left(\frac{h_e^{\,2}}{(1+R)2\eta_i-h_i\,\mathrm{Re}\,h_e}\right)\left(\begin{array}{l}(1+R)\left(\eta_i\left(\frac{(h_{i+1}-2h_i+h_{i-1})}{he^2}\right)+\frac{(h_{i+1}-h_{i-1})}{2he}\right)+\left(\frac{R}{4}\right)\left(\eta_i\left(\frac{(g_{i+1}-g_{i-1})}{2he}+g_i\right)\right)+\\ \mathrm{Re}\left(\left(f_i\left(\frac{(h_{i+1}-h_{i-1})}{2he}\right)\right)-(h_i)^2\right)\end{array}\right) \tag{57}$$

$$g_i = \left(\frac{2h_e^{\,2}}{(4\lambda\eta_i^{\,2} - 4\eta_i\lambda h_e^{\,2}) - \mathrm{Re}\, f_i} \right) \left(\begin{array}{l} \lambda\left(\eta_i^{\,2}\left(\frac{(g_{i+1} - 2g_i + g_{i-1})}{he^2} \right) + 2\eta_i g_i \right) - BR(\eta_i \left(\frac{(f_{i+1} - 2f_i + f_{i-1})}{he^2} \right) + \\ \frac{\eta_i}{2} g_i) - \frac{\mathrm{Re}}{2}\left(2\eta_i (h_i g_i - f_i \left(\frac{g_{i+1} - g_{i-1}}{2h_e} \right) - f_i g_i \right) \end{array} \right) \tag{58}$$

$$\Omega_i = \left(\frac{h_e^{\,2}}{2(1+R)\eta_i} \right) \left((1+R)\left(\eta_i \left(\frac{\Omega_{i+1} + \Omega_{i-1}}{h_e^{\,2}} \right) \right) + \mathrm{Re}\, f_i \left(\frac{\Omega_{i+1} - \Omega_{i-1}}{2h_e} \right) \right) \tag{59}$$

$$\theta_i = \left(\frac{2h_e^{\,2}}{(4\eta_i + 2\beta\eta_i(\theta_{i+1} - 2\theta_i + \theta_{i-1}) + \beta(\theta_{i+1} - \theta_{i-1})} \right) \left(\left(\eta_i \left(\frac{(\theta_{i+1} + \theta_{i+1})}{h_e^{\,2}} \right) + \left(\frac{\theta_{i+1} - \theta_{i-1}}{2h_e} \right) \right) + \beta\eta_i \left(\frac{\theta_{i+1} - \theta_{i-1}}{2h_e} \right)^2 + \mathrm{Re}\,\mathrm{Pr} \left(f_i \left(\frac{\theta_{i+1} - \theta_{i-1}}{2h_e} \right) \right) \right) \tag{60}$$

$$\phi_i = \left(\frac{h_e^{\,2}}{2(1+R)\eta_i} \right) \left(\eta_i \left(\frac{\phi_{i+1} + \phi_{i-1}}{h_e^{\,2}} \right) + \left(\frac{\phi_{i+1} - \phi_{i-1}}{2h_e} \right) \right) + \mathrm{Re}\, Sc \left(f_i \left(\frac{\phi_{i+1} - \phi_{i-1}}{2h_e} \right) \right) \tag{61}$$

The corresponding boundary conditions now become:

$$f_1 = 0, \quad h_1 = 0, \quad \Omega_1 = 0, \quad g_1 = 0, \quad \theta_1 = 0, \quad \phi_1 = 0 \tag{62a}$$

$$h_{81} = 1, \; g_{81} = 0, \quad \Omega_{81} = 1, \quad \theta_{81} = 1, \; \phi_{81} = 1 \tag{62b}$$

The system of equations (56) to (61) with the boundary conditions (62) has been solved iteratively and the FDM results obtained are compared with those obtained by the FEM in **Tables 1, 2 and 3**, showing close agreement.

7. Further Validation with Chebyshev Spectral Collocation Method (SCM)

The eleventh order boundary value problem defined by eqns. (25)-(30) and wall and free stream conditions (31), has also been solved with a spectral collocation method of Chebyshev type (SCM), using a Matlab-based code, Microspecsim, (Micropolar Spectral Simulation) developed for micropolar flows. Again, this is done in order to increase confidence in the FEM and FDM solutions, since inspection of the literature does not yield any practical solutions with which to benchmark our simulations. This technique has been implemented to successfully resolve a number of challenging nonlinear problems. (Bég et al., 2013) simulated

electrohydrodynamic (EHD) ion drag pumping flows at general electrical Hartmann numbers using SCM. (Hoque et al., 2013) analyzed magneto-hydrodynamic blood flow in a curved tube (i.e. the "magnetic Dean problem") using SCM. Further applications include rotating duct heat transfer in aerospace propulsion (Wahiduzzaman et al., 2013). The principal advantage of SCM lies in the accuracy achievable for a given number of unknowns. For problems whose solutions are sufficiently smooth, SCM demonstrates exponential rates of convergence and accuracy. To optimize the present method, Microspecsim has been tested for convergence with respect to the spatial resolution. The solutions converge in 25 iterations in Newton's method. Numerical solutions are found to be independent of the number of collocation points for a sufficiently large number of collocation points. N=65 yields the optimal convergence and very high accuracy (up to 10^{-6}) and is therefore implemented in all the computations in Microspecsim. An excellent perspective of SCM is documented in (Trefethen, 2000). In SCM, we seek an approximate solution, which is a global Chebyshev polynomial of degree N defined on the re-mapped interval [-1, 1]. We discretize the interval by using collocation points to define the Chebyshev nodes in [-1, 1], namely

$$x_j = \cos(\frac{j\pi}{N}), \qquad j = 0.1,2,.....N.. \tag{63}$$

The derivatives of the functions at the collocation points are given by:

$$f^{n}(x_j) = \sum_{j=0}^{N} d_{kj}^{n} f(x_j), \qquad n = 1,2. \tag{64}$$

where d_{kj}^{n} represents the differentiation matrix of order n and are given by

$$d^{1}{}_{kj} = \frac{4\gamma_j}{N} \sum_{n=0}^{N} \sum_{l=0,\, n+l=odd}^{n-1} \frac{n\gamma_n}{c_l} T_l^{n}(x_k) T_n(x_j), \qquad k, j = 0,1,....N, \tag{65}$$

$$d^{2}{}_{kj} = \frac{2\gamma_j}{N} \sum_{n=0}^{N} \sum_{l=0,\, n+l=even}^{n-2} \frac{n\gamma_n (n^2 - l^2)}{c_1} T_l^{n}(x_k) T_n(x_j), \qquad k, j = 0,1,....N, \tag{66}$$

Here $T_n(x_j)$ are the Chebyshev polynomial and the coefficients γ_j and c_l are defined as

$$T_n(x_j = \cos(n\cos^{-1} x_j), \quad \gamma_j = \begin{cases} \frac{1}{2} & j = 0, or\ N \\ 1 & j = 1,2,....N-1 \end{cases} \quad c_l = \begin{cases} 2 & l = 0, or\ N \\ 1 & l = 1,2,....N-1 \end{cases} \tag{67}$$

As described above the Chebyshev polynomials are defined on the finite interval [-1,1]. Therefore, to apply Chebyshev spectral method to the nonlinear boundary eqns. (9)-(11), we make a suitable linear transformation and transform the physical domain [0, ∞] to Chebyshev computational domain [-1, 1]. We sample the unknown function w at the Chebyshev points to obtain the data vector:

$$w = [w(x_0), w(x_1), w(x_2), ...w(x_N),]^T . \tag{68}$$

The next step is to find a Chebyshev polynomial P of degree N that interpolates the data, i.e.

$$P(x_j) = w_j, \quad j = 0,1,...N . \tag{69}$$

and obtain the spectral derivative vector w by differentiating P and evaluating at the grid points, i.e.

$$w'_j = P'(x_j), \quad j = 0,1,...N.. \tag{70}$$

This transforms the nonlinear differential equations into a system nonlinear algebraic equation which are solved by Newton's iterative method starting with a initial guess. The comparisons of FEM and SCM solutions, for skin-friction coefficient and local Nusselt number for the general micropolar model are shown in **Tables 1-3**. Very close agreement is observed, further confirming the accuracy of the FEM solutions, and the FDM solutions.

8. Results and discussion

To study the behavior of the axial velocity, azimuthal velocity, microrotation function, heat and mass transfer functions, we have provided graphs of the parameters namely Reynolds number, micropolar parameter, thermal conductivity parameter and Schmidt number as depicted in figures (1) – (10). Other geometrical and thermophysical parameters namely the Prandtl number, curvature parameter, *B*, and spin gradient viscosity parameter, λ are taken to

be constant at 0.05, 0.1 and 0.5 respectively. The thermal conductivity parameter β has been selected following (Schlichting, 1979) with $\beta > 0$ for air, water etc. and $-0.1 \leq \beta \leq 0$ for lubricating oils. We shall discuss the influence of each parameter on the hydrodynamic regime in turn. The independent variable in the computations, η is the ratio $(r/a)^2$. Hence $\eta = 0$ corresponds to r = 0 i.e. at the center of the cylinder edge; $\eta = 1$ implies that r = a i.e. the surface of the cylinder (near field zone) and $\eta = 41$ corresponds to the far field zone.

8.1 Reynolds Number Effects

Figures (1) – (5) depict the variation of dimensionless axial velocity (h), dimensionless azimuthal velocity (Ω), dimensionless microrotation (g), and dimensionless temperature function (θ) and dimensionless mass transfer function (ϕ) with Reynolds number. Figure (1) illustrates the axial velocity (h) profile for different value of Re. Reynolds number embodies the ratio of inertial force to viscous force. The axial velocity is observed to increase with a fall in Reynolds number; hence the axial momentum is seen to be positively influenced in the stagnation region, by a lower Reynolds number or higher viscous force. For small values of the Reynolds number the axial velocity profile takes a concave shape, indicating that in viscous-dominated flow axial momentum is substantially influenced. As Reynolds number increases, the h profile reduces its concavity i.e. becomes more monotonic. The effect of the Reynolds number on azimuthal velocity is shown in figure 2. Azimuthal velocity increases with a rise in Reynolds number. For larger values of Reynolds number (i.e. 1 and 2) which still correspond to a creeping flow regime, it takes S-shaped but as Re decreases a steep change is obtained. For Re = 0.05, the profile has a monotonic inverted parabolic nature. Variation of the microrotation function, g, with Reynolds number is shown in figure 3. An increase in the Reynold numbers generates a major positive boost in microrotation function especially in the range $0 < \eta < 1$. Also, it is clear from the figure that the concentration of the micro-constituents decreases as Reynolds number rises. With larger values of Re, the angular momentum field is

boosted, increasing the rate of rotation of particles about their poles, leading to a general rise in g values. This result would also be important in assessing the contribution of fluid containing suspension e.g. sediment-laden water on the ocean bed. Figures 4-5 display the distribution of temperature and mass transfer function. As the Reynolds number increases, the temperature function, θ, and mass transfer function, ϕ, decrease continuously with distance from the cylinder end center ($\eta = 0$) i.e. further into the pure fluid regime (free stream). Temperature profiles are seen to decay monotonically from the cylinder end center where $\eta = 0$, to the far field zone i.e. where $\eta \rightarrow \infty$ (41 in the case of the present numerical computations). The rate of descent of the θ profiles is much sharper however for larger Re values (0.5, 1, 2) than for the lowest Re value (0.05). For the case of the mass transfer function, (figure 5), the ϕ profiles also decay but less sharply than temperature profiles. In both figures a very low Prandtl number has been used (Pr = 0.05) which could characterize a liquid metal ambient fluid or heavily sediment-laden suspension i.e. hyper-concentrated flow. The Schmidt number Sc is set at 1.0. This parameter defines physically the ratio of momentum diffusivity (viscosity) and mass diffusivity. For a unity value both momentum and species diffuse at the same rate. Prandtl number however defines the ratio of momentum diffusivity to thermal diffusivity implying that for Pr = 0.05 i.e. heat conduction is very effective compared to convection: thermal diffusivity is dominant. For larger Pr fluids e.g. molten chocolate, creams etc, convection is very effective in transferring energy from an area, compared to pure conduction i.e. in this case momentum diffusivity is dominant. The Prandtl number controls the relative thickness of the momentum and thermal boundary layers. Reynolds number has a much less dramatic effect on mass transfer field compared with the thermal field. ϕ values are reduced as Re increases from 0.05 to 2 but only marginally.

8.2 Micropolarity Effects

Figures 6 – 8 illustrate the distribution of axial velocity, azimuthal velocity and microrotation function with the effect of micropolar parameter, R. The results for R = 0 correspond to a Newtonian viscous fluid. Figure 6 indicates that axial velocity, h, increases with an elevation in the micropolar parameter, R; profiles also reduce in their curviness as R increases. R defines the ratio of the vortex (micropolar) viscosity to the product of fluid density and Newtonian kinematic viscosity. It is observed that velocity for Newtonian (Navier-Stokes viscous fluid, R = 0) is noticeably less than the micropolar fluid cases (R > 0). This physically implies that by the addition of more and more microconstituents to the fluid, axial velocity can be increased. Such a characteristic may be exploited in industrial operations. Figure 7 depicts the effect of micropolar parameter, R, on the azimuthal velocity. Azimuthal velocity decreases as the micropolar parameter increases from 0 to 3. Profiles assume S-shaped configurations for the different values of micropolar parameter, R; a steep increase in velocity is witnesses in the vicinity of the boundary i.e. at $\eta = 0$ (cylinder edge center). Microrotation function, g, versus η, is illustrated in figure 8, for different values of micropolar parameter, R. g is seen to increase in magnitude with a rise in the micropolar parameter. For R = 0 the peak magnitude of g at $\eta = 0$ is about 0.025; for R = 3.0 it is 0.037. As expected, near the boundary ($\eta = 0$) a fast change is observed i.e. a sharp rate of change of micro-rotation or micro-rotation gradient ($dg/d\eta$) is seen here. In the free stream, the gradient however decreases, and the profiles tend very smoothly (almost horizontally in the case of R = 0 i.e. Newtonian fluid) to zero. It therefore appears that micro-rotation is greater in the fluid regime nearer the cylinder edge and curved surface but decays considerably in the far field zone.

8.3 Thermal Conductivity Variation Effects

Figures 9 illustrates the temperature function, θ, distributions with η. Figure 9 shows the effect of thermal conductivity parameter, β, on temperature function. Temperature increases as the

thermal conductivity parameter increases. The characteristic of variable thermal conductivity is very common in many engineering processes encountered in the metallurgical and chemical processing industries e.g. enrobing, gold-plating, electroplating etc. Where temperature attains very high values, the thermal conductivity parameter can be used to control the temperature fields. We also observe that the rate of change of temperature function ($d\theta/d\eta$) is very high in the region $0 < \eta < 11$, at which θ values become zero instantaneously.

8.4 Schmidt Number Effects

Figure 10 illustrates the mass transfer profile for different value of Schmidt number. Schmidt number regulates the mass diffusion phenomena in the flow regime. Schmidt number as defined earlier represents the ratio of momentum diffusivity to the molecular diffusivity. As the Schmidt number increases, from 0.5 (species diffuses twice as fast as momentum) to 3 (momentum diffuses at 3 times the rate of species), the mass transfer function, ϕ, decreases; however, for moderate value of the Schmidt number it decreases slowly i.e. Sc = 0.5 the decrease is much more gradual than for higher values.

We have also tabulated in Table 1 the variation of the skin friction and heat transfer with respect to Reynolds number, micropolar parameter and thermal conductivity parameter. Our computations obtained with both finite element and finite difference methods, show that the skin friction coefficient increases with a rise in Reynolds number and surface parameter but falls with an increase in micropolar parameter. The rate of heat transfer is depressed with rising thermal conductivity parameter (β) and surface parameter (s) but conversely boosted with an increase in the Reynolds number. An increase in the heat transfer rate implies faster cooling of the cylinder surface. Thus, the rate of heat transfer can be controlled effectively by regulating the thermal conductivity parameter.

9. Conclusions

A mathematical model has been presented for the micropolar heat, mass and momentum transfer in the stagnation region of an infinitely long horizontal cylinder, using Eringen's micro-continuum theory and boundary layer physics. Both finite element and finite difference computations have been performed. The simulations indicate that:

- The axial velocity increases with a decrease in the Reynolds number and micropolar parameter.
- Thermal conductivity parameter (β) and Reynolds number (Re) can be used effectively for controlling the rise in the temperature.
- Skin friction increases with increase in Reynolds number but decreases with micropolar parameter.
- Heat transfer rate decreases with an increase in the thermal conductivity parameter and surface parameter whereas it is elevated with Reynolds number.
- With higher Reynolds number, micro-rotation (angular velocity) values are enhanced.
- With greater Schmidt number the mass transfer function (species concentration) decreases. The rate of heat transfer is depressed with rising thermal conductivity parameter
- The rate of heat transfer thus can be regulated by the conductivity parameter which can be exploited in commercial metallurgical operations and also may have significance in ocean pipeline bed contamination releases near hydrothermal vents.

FEM has been shown to provide excellent stability and accuracy for non-linear stagnation point micropolar enrobing flow simulations. The technique, again based on the variational formulation, is presently being applied to consider nonlinear micropolar nanofluid transport from cylindrical curved bodies (Prasad et al., 2015) and also heat and mass transfer from rotating and spherical or conical bodies (Bég et al., 2015; Bég et al., 2012). The results of these investigations will be communicated imminently.

Acknowledgments

The authors are grateful to both reviewers for their comments which have served to improve the article.

References

Baag, S., Mishra, S.R., Dash, G.C., Acharya, M.R., Numerical investigation on MHD micropolar fluid flow toward a stagnation point on a vertical surface with heat source and chemical reaction, *Journal of King Saud Engineering Sciences*., Vol. **29**, pp. 75-83, 2017.

Bean, M.J., Manufacturing processes, Enrobing, Science and Technology of Enrobed and Filled Chocolate, Confectionery and Baked Products, Ed. G. Talbot, Woodhead Publishing in Food Science, Technology and Nutrition, UK, pp. 362-396, 2009.

Bég, O. Anwar, Bhargava, R., Rawat, S., Takhar, H.S., and Halim, M.K., Computational modeling of biomagnetic micropolar blood flow and heat transfer in a two-dimensional non-Darcian porous medium, *Meccanica.*, vol. **43**, no. 4, pp. 391-410, 2008.

Bég, O. Anwar, Bakier, A.Y., and Prasad, V.R., Numerical study of free convection magnetohydrodynamic heat and mass transfer from a stretching surface to a saturated porous medium with Soret and Dufour effects, *Comput. Mat. Sci.*, vol. **46**, no. 1, pp. 57-65, 2009.

Bég, O. Anwar, Bhargava, R., and Rashidi, M.M., *Numerical Simulation in Micropolar Fluid Dynamics*, Germany: Lambert, Sarbrucken, 2011.

Bég, O. Anwar, Hameed, M., and Bég, T.A., Chebyshev spectral collocation simulation of nonlinear boundary value problems in electrohydrodynamic, *Int. J. Comput. Methods in Eng. Sci. Mech.*, vol. **14**, pp. 104-115, 2013.

Bég, O. Anwar, Mabood, F., and Islam, M.N., Homotopy simulation of nonlinear unsteady rotating nanofluid flow from a spinning body, *Int. J. Eng. Math.*, Article ID:272079 (15 pages), 2015.

Bég, O. Anwar, Zueco J., and Chang, T.B., Numerical analysis of hydromagnetic gravity-driven thin film micropolar flow along an inclined plane, *Chem. Eng. Commun.*, vol. **198**, no. 3, pp. 312-331, 2010.

Bég, T.A., Bég, O. Anwar, Rashidi, M.M., and Asadi, M., Homotopy semi-numerical modelling of nanofluid convection flow from an isothermal spherical body in a permeable regime, *Int. J. Microscale and Nanoscale Thermal and Fluid Transport Phenomena.*, vol. **3**, no. 4, pp. 67-96, 2012.

Cunningham, F.E., *Developments in Enrobed Products*, *Processing of Poultry*, Chapter 10, pp. 325-359, USA: Chapman and Hall, 1995.

Das, M., Jain, V.K., and Ghoshdastidar, P.S., Computational fluid dynamics simulation and experimental investigations into the magnetic field assisted nano-finishing process, *Proc. IMechE Part B: J Eng. Manufacture.*, vol. **226**, pp. 1143-1158, 2012.

Deen, W.M., Analysis of Transport Phenomena, UK: Oxford University Press, 1998.

Dietl, C., Winter, E.R.F., and Viskanta, R., An efficient simulation of the heat and mass transfer processes during drying of capillary porous, hygroscopic materials, *Int. J. Heat and Mass Transfer.*, vol. **41**, pp. 3611-3625, 1998.

Dowding, C.F., and Lawrence, J., Use of thin laminar liquid flows above ablation area for control of ejected material during excimer machining, *Proc. IMechE Part B: J. Eng. Manufacture.*, vol. **223**, pp. 759-773, 2009.

Edwards, D.A., and Brenner, H., Interfacial Transport Processes and Rheology, USA: Butterworths, 1993.

Eringen, A. C., Theory of micropolar fluids, *J. Math. Mech.*, vol. **16**, pp. 1-18, 1966.

Eringen, A.C., *Micro-continuum Field Theories, Volume II: Fluent Media*, New York: Springer-Verlag, 2002.

Eringen, A.C., Simple microfluids, *Int. J. Eng. Sci.*, vol. **2**, pp. 200-207, 1964.

Eringen, A.C., Theory of thermomicrofluids, *Math. Anal. Applic. J.*, vol. **38,** 480-496, 1972.

Fedorov, A.G., and Viskanta, R., Combined heat and mass transfer and adsorption dynamics in the microchannel adsorption reactor, *Microscale Thermophysical Eng.*, vol. **3**, no. 2, pp. 111-140, 1999.

Fedorov, A.G., and Viskanta, R., Heat and mass transfer and adsorption dynamics in a honeycomb absorbent: application of the simplified local density model, *Thermal Sci. Eng. J.*, vol. **6**, no. 1, pp. 1-9, 1998.

Ghaly, A.Y., Seddeek, M.A., Chebyshev finite difference method for the effect of reaction, heat and mass transfer on laminar flow along a semi-infinite horizontal plate with temperature dependent viscosity, *Chaos, Solitons and Fractals,* vol. **19**, pp. 61-70, 2004.

Gorla, R.S.R., and Hassanien, I.A., Mixed convection boundary layer flow of a micropolar fluid near a stagnation point on a horizontal cylinder, *Int. J. Eng. Sci.,* vol. **28**, pp. 153-161,1990.

Gray, M.P., *Moulding, enrobing and cooling chocolate products,* Chapter 14, Industrial Chocolate Manufacture and Use, UK: Wiley Blackwell, Oxford, 2009.

Grigoropoulos, C.P., Bennett, T.D., Ho, J.R., Xu, X., and Zhang, X., Heat and mass transfer in pulsed-laser-induced phase transformation, *Adv. Heat Transfer.,* vol. **28**, pp. 75-134, 1996.

Gupta, D., Kumar, L., Bég, O. Anwar, and Singh, B., Finite element simulation of mixed convection flow of micropolar fluid over a shrinking sheet with thermal radiation, *Proc. IMechE Part E: J. Process Mech. Eng.,* vol. **228**, pp. 61-72, 2014.

Hassanien, I.A., and Salma, A.A., Flow and heat transfer of a micropolar fluid in an axisymmetric stagnation flow on a cylinder, *Energy Convers. Mgmt.,* vol. **38**, pp. 301-310, 1997.

Hoque, M.M., Alam, M.M., Ferdows, M., and Bég, O. Anwar, Numerical simulation of Dean number and curvature effects on magneto-biofluid flow through a curved conduit, *Proc. IMechE-Part H: J. Eng. Medicine.,* vol. **227**, pp. 1155-1170, 2013.

Hoyt, J.W., and Fabula, A. G., *The effect of additives on fluid friction, U.S. Naval Ordinance Test Station Report,* United States Navy, Delaware, USA, 1964.

Iqbal, Z., Mehmood, R., Azhar, E., Mehmood, Z., Impact of inclined magnetic field on micropolar Casson fluid using Keller box algorithm, *The European Physical Journal Plus*, Vol. **132**, 2017.https://doi.org/10.1140/epjp/i2017-11443-7.

Kelson, N.A., and Farrell, T.W., Micropolar flow over a porous stretching sheet with strong suction or injection, *Int. Comm. Heat Mass Transfer.,* vol. **28**, pp. 479-488, 2001.

Mansour, M.A., El-Hakiem, M.A., and El Kabeir, S.M., Heat and mass transfer in magneto-hydrodynamic flow of micropolar fluid on a circular cylinder with uniform heat and mass flux, *J. Magnetism Magnetic Materials.,* vol. **220**, pp. 259-270, 2000.

Mehmood, Z., Mehmood, R., Iqbal, Z., Numerical investigation of micropolar Casson fluid over a stretching sheet with internal heating, *Communications in Theoretical Physics*, Vol. **67**(4), pp. 443-448, 2017.

Mehmood, R., Nadeem, S., Masood, S., Effects of transverse magnetic field on a rotating micropolar fluid between parallel plates with heat transfer, *Journal of Magnetism and Magnetic Materials*., Vol. **401**, pp. 1006-1014, 2016.

Mihic, S.D., Cioc, S., Marinescu, I.D., Weismiller, M.C., Detailed study of fluid flow and heat transfer in the abrasive grinding contact using computational fluid dynamics methods, *ASME J. Manufacturing Sci. Eng.*, vol.**135**, Article ID: 041002, (13 pages), 2013.

Mishra, S.R., Dash, G.C., Pattnaik, P.K., Flow of heat and mass transfer on MHD free convection in a micropolar fluid with heat source, *Alexandria Engineering Journal*., Vol. **54** (3), pp. 681-689, 2015.

Mishra, S.R., Baag, S., Mohapatra, D.K., Chemical reaction and Soret effects on hydromagnetic micropolar fluid along a stretching sheet, *Engineering Science and Technology, an International Journal*, Vol. **19**(4), pp. 1919-1928, 2016.

Parthasarathy, A., and Malkin, S., Effect of fluid application conditions on grinding behaviour, *Proc. IMechE Part B: J Eng. Manufacture.*, vol. **224**, pp. 225-235, 2010.

Prasad, V.R., Gaffar, S.A., and Bég, O. Anwar, Heat and mass transfer of a nanofluid from a horizontal cylinder to a micropolar fluid, *AIAA J. Thermophysics Heat Transfer.*, vol. **29**, no. 1, pp. 127-139, 2015.

Rana, P., Bhargava, R., and Bég, O. Anwar, Finite element modelling of conjugate mixed convection flow of Al_2O_3-water nanofluid from an inclined slender hollow cylinder, *Physica Scripta*, vol. 87, no.5, 055005, (15 pages), 2013b.

Rana, P., Bhargava, R., and Bég, O. Anwar, Finite element simulation of unsteady magneto-hydrodynamic transport phenomena on a stretching sheet in a rotating nanofluid, *Proc. IMechE: Part N: J. Nanoengineering and Nanosystems*, vol. **227**, pp. 277-299, 2013a.

Rashidi, M.M., Ferdows, M., Uddin, M.J., Bég, O. Anwar, and Rahimzadeh, N., Group theory and differential transform analysis of mixed convective heat and mass transfer from a horizontal surface with chemical reaction effects, *Chem. Eng. Commun.*, vol. **199**, pp. 1012-1043, 2012.

Rashidi, M.M., Keimanesh, M., Bég, O. Anwar and Hung, T.K., Magnetohydrodynamic biorheological transport phenomena in a porous medium: A simulation of magnetic blood flow control and filtration, *Int. J. Numer. Methods in Biomedical Eng.*, vol. **27**, pp. 805–821, 2011.

Rawat, S., Bhargava, R., Bhargava, Renu, Bég, O. Anwar, Transient magneto-micropolar free convection heat and mass transfer through a non-Darcy porous medium channel with variable thermal conductivity and heat source effects, *Proc. IMechE Part C- J. Mech. Eng. Sci.*, vol. **223**, pp. 2341-2355, 2009.

Reddy, J.N., *An Introduction to the Finite Element Method*, New York: McGraw-Hill Book Co., 1985.

Rout, P.K., Sahoo, S.N., Dash, G.C., Mishra, S.R., Chemical reaction effect on MHD free convection flow in a micropolar fluid, *Alexandria Engineering Journal*., Vol. **55**(3), pp. 2967-2973, 2016.

Schlichting, H., *Boundary Layer Theory*, New York: Mac-Graw-Hill (6^{th} Edn.), 1979.

Tan, W., Bailey, N.S., Shih, Y.C., Numerical modeling of transport phenomena and dendritic growth in laser spot conduction welding of 304 stainless steel, *ASME J. Manufacturing Sci. Eng.*, vol. **134**, Article ID:041010, (15 pages), 2012.

Tien, C.L., and Campbell, D.T., Heat and mass transfer from rotating cones, *J. Fluid Mech.*, vol. **17**, pp. 105-112, 1963.

Trefethen, N.L., *Spectral Methods in MATLAB*, USA: SIAM Press, 2000.

Uddin, M.J., Yusoff, N.H.M., Bég, O. Anwar and Ismail, A.I.M, Lie group analysis and numerical solutions for non-Newtonian nanofluid flow in a porous medium with internal heat generation, *Physica Scripta*, vol. **87**, Article ID:025401, 2013.

Wahiduzzaman, M., Alam, M.M., Ferdows, M., Sivasankaran, S., and Bég, O. Anwar, Spectral numerical study of non-isothermal flow in a rotating rectangular cross-section duct, *Int. J. Appl. Math and Mech.*, vol. **9**(24), pp. 1-18, 2013.

Zueco, J., Bég, O. Anwar, Takhar, H.S., Network numerical analysis of magneto-micropolar convection through a vertical circular non-Darcian porous medium conduit, *Comput. Materials Sci.*, vol. **46**, no. 4, pp. 1028-1037, 2009.

TABLES

Table 1: Comparison of FEM, FDM and SCM solutions for skin friction and heat transfer rate with various Reynolds numbers (Re) [$s = 0.5,\ \lambda = 1.0,\ \Pr = 1.0, B = 0.1, R = 0.1, Sc = 1.0, \beta = 0.3$].

Re	$-f''(0)$ FEM	$-f''(0)$ FDM	$-f''(0)$ SCM	$-\theta(0)$ FEM	$-\theta(0)$ FDM	$-\theta(0)$ SCM
0.05	-0.134636	-0.134635	-0.134636	0.221291	0.221292	0.221291
0.5	-0.072500	-0.072501	-0.072500	0.380056	0.380055	0.380055
1.0	-0.051311	-0.051310	-0.051311	0.435477	0.435476	0.435478
2.0	-0.041134	-0.041133	-0.041134	0.465138	0.465137	0.465137

Table 2: Comparison of FEM, FDM and SCM solutions for skin friction and heat transfer rate with various micropolar parameters (R) [$s = 0.5,\ \lambda = 1.0,\ \Pr = 1.0, B = 0.1, \mathrm{Re} = 1, Sc = 1.0, \beta = 0.3$].

R	$-f''(0)$ FEM	$-f''(0)$ FDM	$-f''(0)$ SCM	$-\theta(0)$ FEM	$-\theta(0)$ FDM	$-\theta(0)$ SCM
0	-0.058804	-0.058803	-0.058805	0.459696	0.459695	0.459698
1	-0.065023	-0.065022	-0.065025	0.478699	0.478697	0.478698
2	-0.072874	-0.072871	-0.072873	0.501579	0.501576	0.501580
3	-0.077873	-0.077874	-0.077875	0.515571	0.515568	0.515572

Table 3: Comparison of FEM, FDM and SCM solutions for skin friction and heat transfer rate with various surface parameters (S) [$\lambda = 1.0,\ \Pr = 1.0, B = 0.1, \mathrm{Re} = 1, R = 0.1, Sc = 1.0, \beta = 0.3$].

s	$-f''(0)$ FEM	$-f''(0)$ FDM	$-f''(0)$ SCM	$-\theta(0)$ FEM	$-\theta(0)$ FDM	$-\theta(0)$ SCM
0.0	-0.034827	-0.034826	-0.034826	0.484482	0.484480	0.484481
0.25	-0.034588	-0.034587	-0.034586	0.484594	0.484590	0.484592
0.5	-0.034891	-0.034894	-0.034892	0.484762	0.484759	0.484763
0.75	-0.034923	-0.034927	-0.034924	0.484887	0.484879	0.484889
1.0	-0.034955	-0.034951	-0.034957	0.485041	0.485038	0.485040

Table 4: Comparison of FEM, FDM and SCM solutions for skin friction and heat transfer rate with various thermal conductivity parameters (β)

[$\lambda = 1.0,\ \Pr = 1.0, B = 0.1, \mathrm{Re} = 1, R = 0.1, Sc = 1.0, s = 0.5$].

β	$-f''(0)$ FEM	$-f''(0)$ FDM	$-f''(0)$ SCM	$-\theta(0)$ FEM	$-\theta(0)$ FDM	$-\theta(0)$ SCM
0.05	-0.051311	-0.051309	-0.051311	0.591326	0.591322	0.591325
0.0	-0.051311	-0.051309	-0.051311	0.566993	0.566990	0.566992
0.3	-0.051311	-0.051309	-0.051311	0.435477	0.435474	0.435475
1.0	-0.051311	-0.051309	-0.051311	0.170602	0.170600	0.170601
1.5	-0.051311	-0.051309	-0.051311	-0.123647	-0.123642	-0.123647

FIGURE CAPTIONS

Schematic. 1: Physical model and coordinate system

Figure. 1: Axial Velocity for different Re (R=0.5, Sc=1.0)

Figure. 2: Azimuthal velocity for different Re (R=0.5, Sc=1.0).

Figure. 3: Microrotation for different Re (R=0.5, Sc=1.0).

Figure. 4: Temperature for different Re (R=0.5, Sc=1.0)

Figure. 5: Mass transfer for different Re (R=0.5, Sc=1.0)

Figure. 6: Axial velocity for different R (Re=0.5, Sc=1.0)

Figure. 7: Azimuthal velocity for different R (Re=0.5, Sc=1.0)

Figure. 8: Microrotation for different R (Re=0.5, Sc=1.0)

Figure. 9: Temperature for different β (Re=0.5, R=0.5, Sc=1.0)

Figure. 10: Mass transfer for different Sc (Re=0.5, R=0.5, β =1.0)

SCHEMATICS AND FIGURES

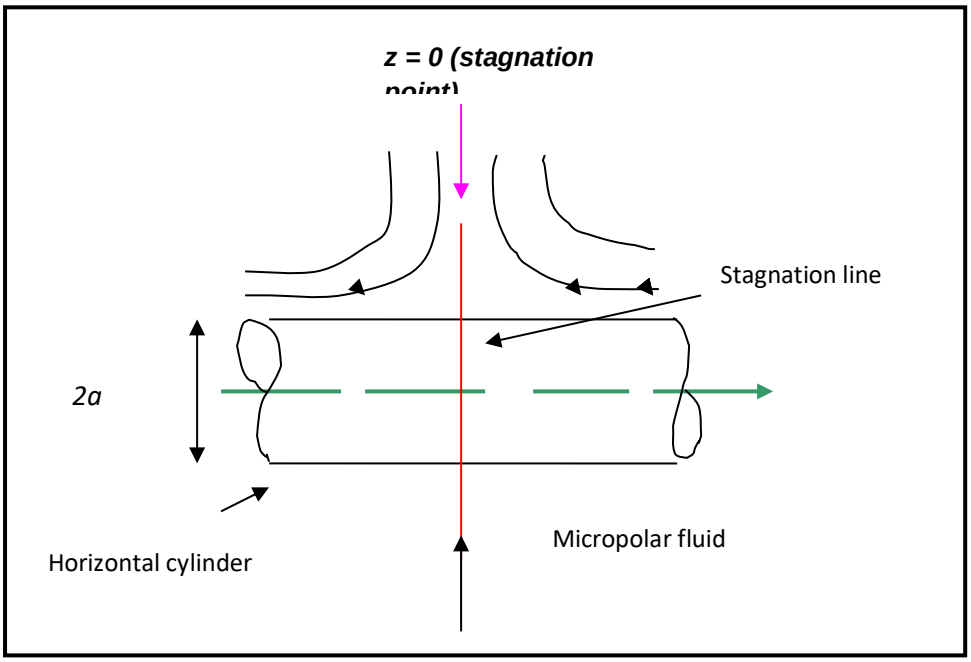

Schematic. 1: Physical model and coordinate system

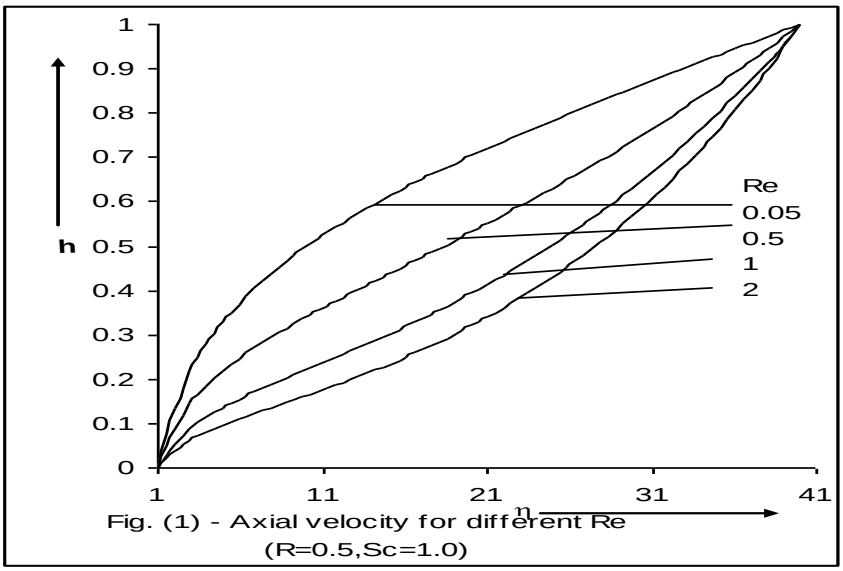

FIG. 1: Axial Velocity for different Re (R=0.5, Sc=1.0)

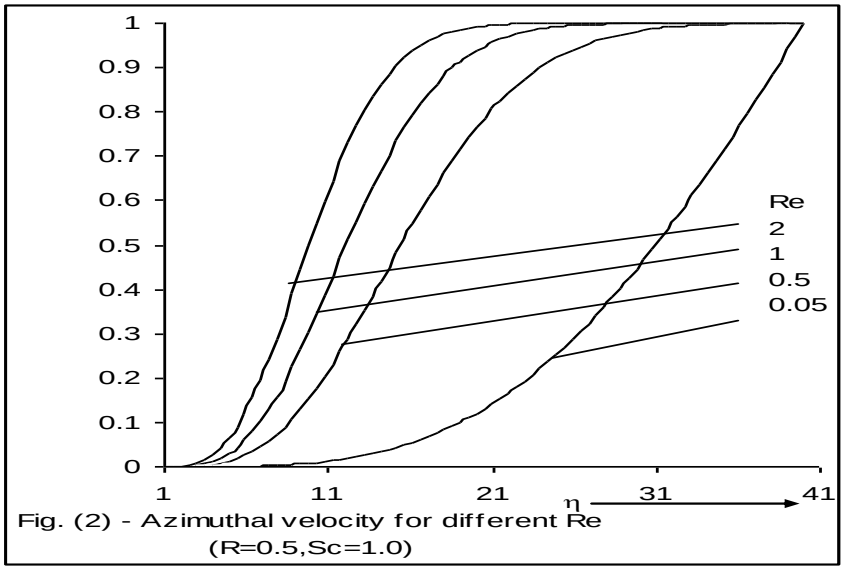

FIG. 2: Azimuthal velocity for different Re (R=0.5, Sc=1.0)

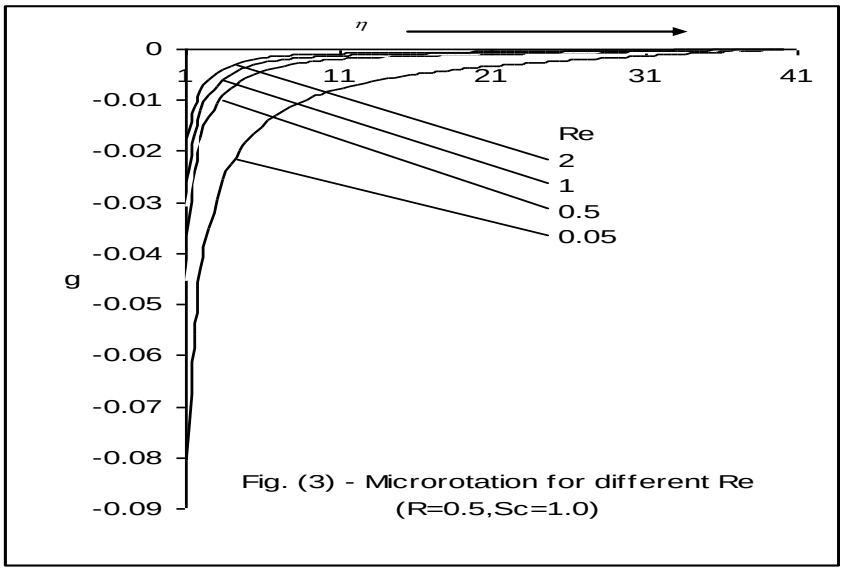

FIG. 3: Microrotation for different Re (R=0.5, Sc=1.0)

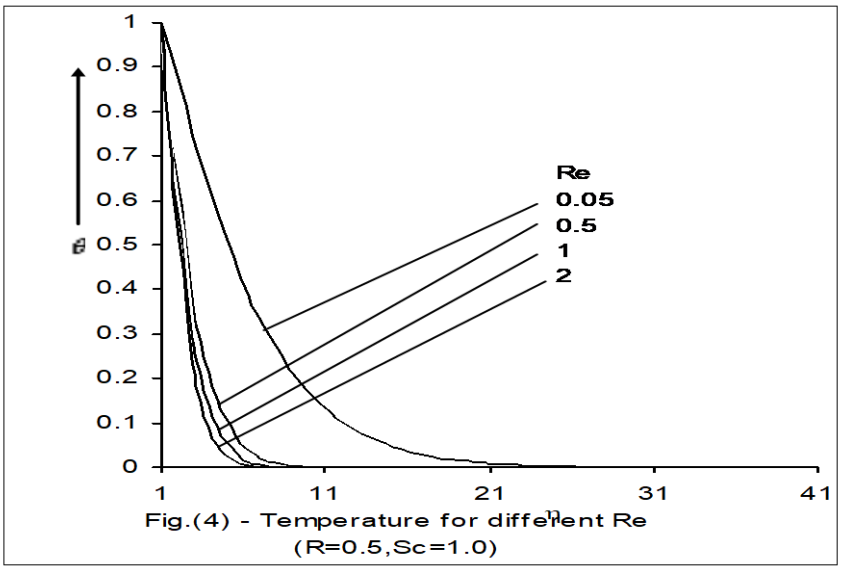

FIG. 4: Temperature for different Re (R=0.5, Sc=1.0)

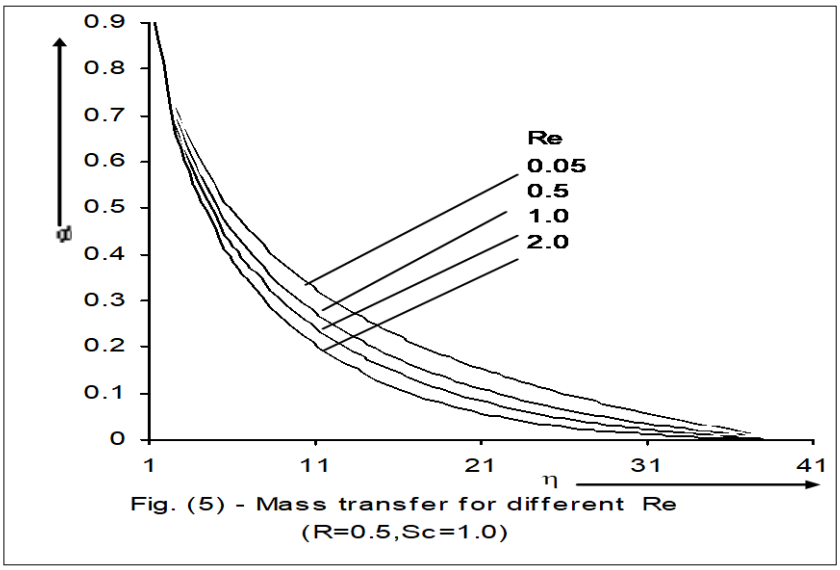

FIG. 5: Mass transfer for different Re (R=0.5, Sc=1.0)

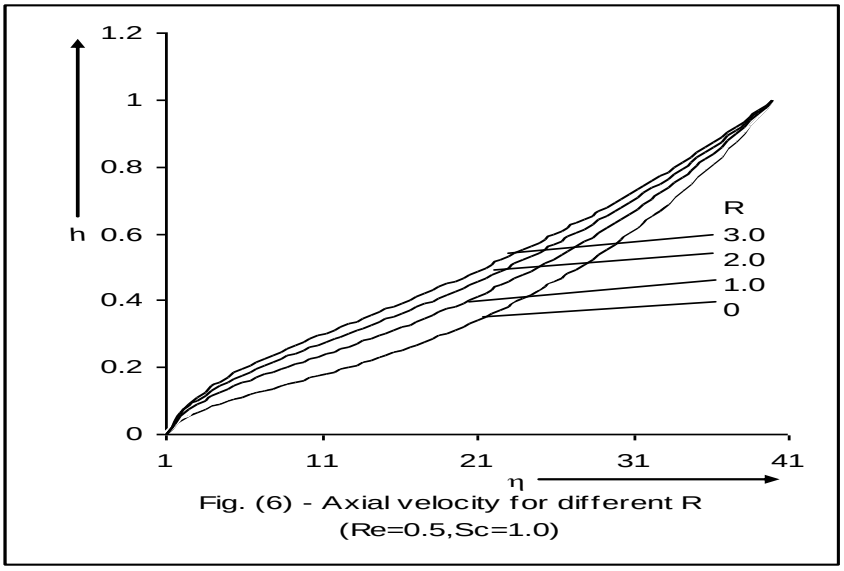

FIG. 6: Axial velocity for different R (Re=0.5, Sc=1.0)

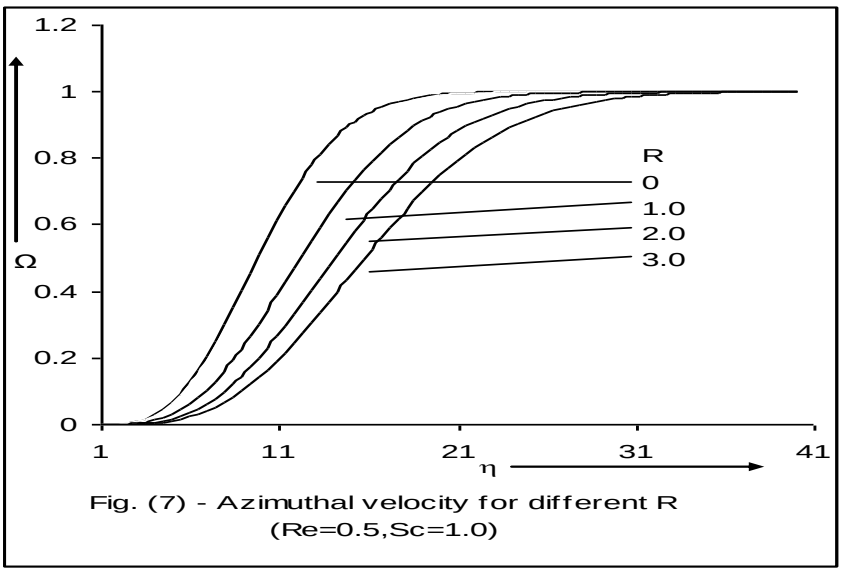

FIG. 7: Azimuthal velocity for different R (Re=0.5, Sc=1.0)

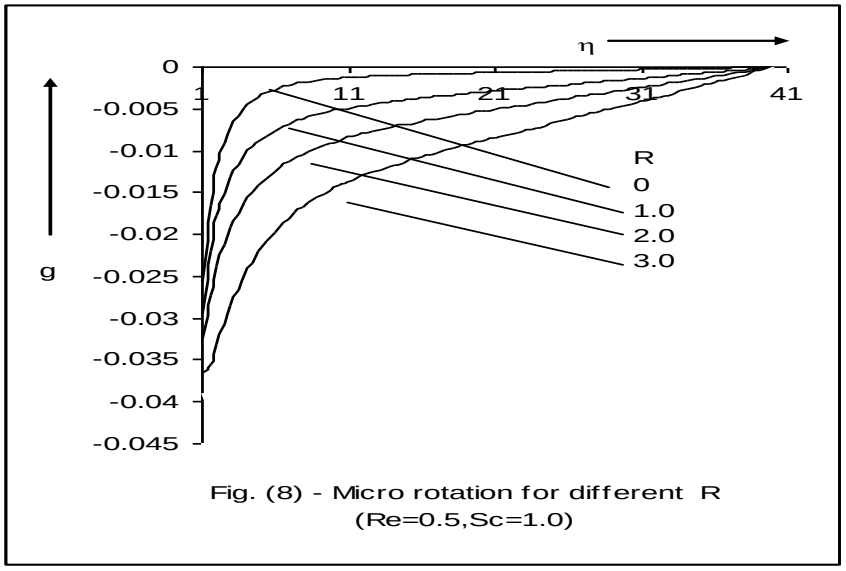

FIG. 8: Microrotation for different R (Re=0.5, Sc=1.0)

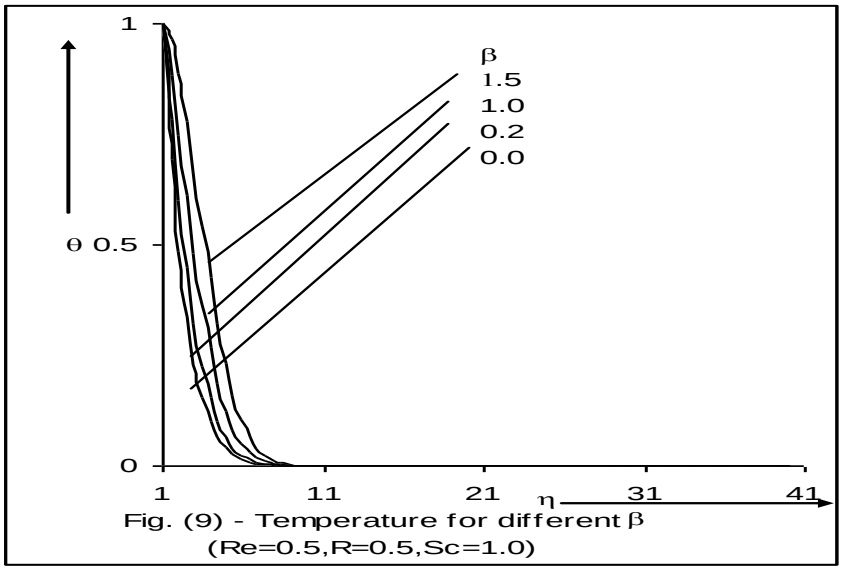

FIG. 9: Temperature for different β (Re=0.5, R=0.5, Sc=1.0)

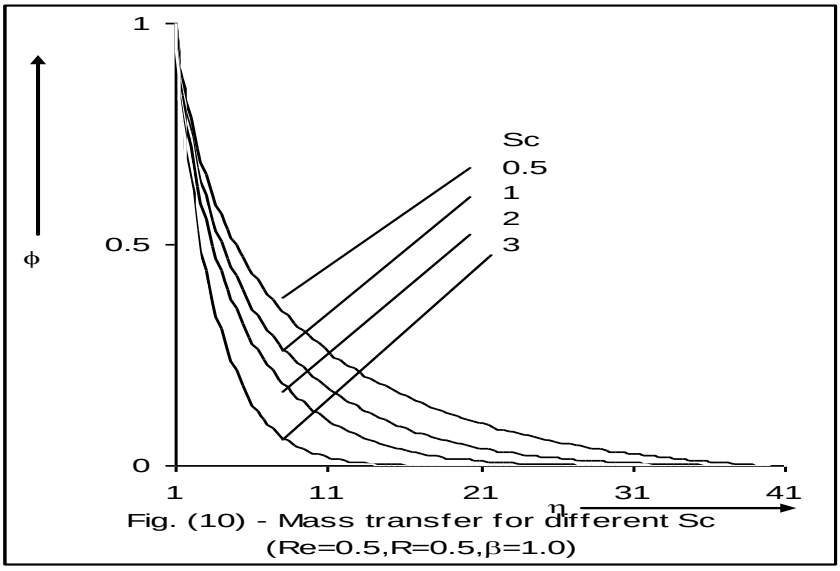

FIG. 10: Mass transfer for different Sc (Re=0.5, R=0.5, β =1.0)